HCN channels regulate excitability and gate synaptic amplification via NMDA in mouse L2/3 pyramidal neurons

Viktor János Oláh[1], Jing Wu[2], Leonard K. Kaczmarek[2,3] & Matthew JM Rowan[1,4*]

[1]Department of Cell Biology, Emory University School of Medicine, Atlanta, GA, 30322, USA
[2]Department of Pharmacology, Yale University School of Medicine, New Haven, Connecticut 06520
[3]Department of Cellular and Molecular Physiology, Yale University School of Medicine
[4]Center for Neurodegenerative Disease, Emory University School of Medicine

***Address for Correspondence:**
Matt Rowan, PhD
Emory University School of Medicine
Department of Cell Biology
Atlanta, GA, 30322
Email: mjrowan@emory.edu

Citations: 72; *Figures*: 7 main figures; 4 supplementary figures

ABSTRACT

Layer 2/3 pyramidal cells (L2/3 PCs) play a crucial role in cortical information transfer. Although the dendritic arbors of L2/3 PCs are impressive, they lack the distinct anatomical compartments characteristic of deeper L5 PCs. For example, many L2/3 PCs do not display an apparent distal tuft region. However, L2/3 PCs receive inputs from both thalamic (bottom-up) and cortical (top-down) inputs, preferentially synapsing onto their proximal and distal dendrites, respectively. Nonuniform organization of channels and NMDA receptors in L2/3 dendrites could serve to independently modulate these information streams to affect learning and behavior, yet whether L2/3 PC dendrites possess this capability has not been established. Here, we found a previously unappreciated non-uniform HCN channel distribution in L2/3 PCs, allowing for pathway-specific gating of NMDA receptor recruitment at bottom-up (proximal) but not top-down (distal) synapses. Interestingly, HCN availability could be regulated via neuromodulation, suggesting that the gain of thalamic and cortical-cortical signals in L2/3 may be independently modified *in vivo*.

INTRODUCTION

Layer 2/3 pyramidal cells (L2/3 PCs) are the most numerous excitatory neurons in the neocortex. As a major component of the canonical circuit, L2/3 PCs are thought to play crucial roles in information transfer and gain control of cortical output(1). Thus, disambiguating the afferent circuit connections of L2/3 PCs has been a significant focus of neuroscience research in the past decade(2-5). However, understanding cellular mechanisms by which L2/3 PCs transform information is equally important (6-9). Like their more extensively studied counterparts (e.g., L5 PCs, hippocampal CA1 PCs), L2/3 PCs are equipped with an array of dendritic nonlinearities(10, 11), enabling complex subcellular computations. Nonetheless, L2/3 PCs exhibit marked disparities from other PC types as well. Their morphology is less segmented, due to the lack of a distinctive apical tuft (except for deep layer 3 cells (12)). Their dendritic protrusions are also shorter, and consequently possess less surface area over which specialized nonlinear operations may be actualized. Therefore, the applicability of currently established neuronal dynamics to L2/3 PCs is questionable.

Dendritic voltage-gated channels and receptors are crucial for diversifying the computational power of neuronal cells, by allowing for nonlinear processing of arriving synaptic inputs(13). Nonlinear processing is essential for proper brain function and has been implicated in critical tasks such as conscious perception(14, 15) and processing of sensory and motor input(16). Therefore, a more comprehensive understanding of subcellular signal processing dynamics in L2/3 PCs is warranted. Dendritic hyperpolarization-activated nonselective cation (HCN) channels are a staple of several PC classes(17, 18), playing essential roles in regulating resting membrane potential, the normalization of synaptic events arriving at spatially mismatched locations, and establishing oscillation frequency-selectivity(19). Beyond exerting control over the general excitability of neurons, HCN channels contribute to synaptic plasticity and regulate working memory(19). In following, HCN dysfunction contributes to mechanisms of epilepsy and pain(20). Electrophysiological detection of this current often relies on identification of a characteristic 'sag' potential, elicited by hyperpolarizing current injections. In L2/3 PCs, this sag potential is negligible in most cortical areas (but see (21)) thus, HCN channels are often stated as missing from L2/3 PCs. Therefore, the functional expression of HCN channels in these cells remains ambiguous.

Here we report that L2/3 PCs throughout the cortex express functionally relevant HCN channels with surprising functions. We found that HCN channels robustly influence the overall excitability of L2/3 PCs. Interestingly, we found that HCN channel availability in L2/3 PCs is biased in a unique proximal somato-dendritic manner, which is inverted with respect to L5 and hippocampal CA1 PCs, where HCN is enriched within their distal apical tufts(18, 22). In cooperation with NMDA receptors, this L2/3 HCN organization could modulate the boosting of proximal 'bottom-up' dendritic

inputs, without affecting distal 'top-down' dendritic inputs. Furthermore, we found that HCN expression is robustly upregulated during early postnatal development and that neuromodulation in adulthood can rapidly adjust HCN channel availability. Our results demonstrate that L2/3 PCs not only express dendritic HCN channels, but also employ these conductances in a previously unappreciated manner.

RESULTS

HCN channel expression in L2/3 PCs

HCN channels have been extensively documented and rigorously characterized in several cortical PC types(17), however, whether PCs residing in layer 2/3 of the mouse cortex express functionally relevant HCN channels remains ambiguous. Nonetheless, open-source snRNAseq (23) shows comparable HCN subunit mRNA levels in all cortical PC types of the visual cortex (Fig. 1a). Therefore, we investigated whether this mRNA signature translated to HCN surface expression. Immunohistochemical staining against HCN1 showed discernible somatic fluorescent signal in many cells residing in superficial layers of the cortex (Fig. 1b) along with staining of putative dendrites. To examine the potential functional role for HCN channels in L2/3 PCs, we performed *ex vivo* cell-attached recordings from visually identified L2/3 PCs in the primary visual cortex from mature mice. Spike output upon extracellular stimulation (50 Hz) in layer 4 was then measured in control conditions and following pharmacological HCN channel block (Fig. 1c). We found that bath application of Cs^+ (2mM), a conventional blocker of HCN channels at this concentration, significantly increased their firing (Fig. 1d). This was unlikely due to presynaptic modulation of these synapses, as the paired-pulse ratio was unchanged in a set of separate whole-cell recordings coupled with stimulation in layer 4 (Fig. 1e). Together, these results suggest that L2/3 PCs express a functionally relevant set of HCN channels which limit excess AP firing following synaptic stimulation.

HCN channels constrain the overall excitability of L2/3 PCs

To investigate the role of HCN channels in regulating the excitability of L2/3 PCs, we next performed further L2/3 PC whole-cell recordings. A conventionally used assessment of HCN channel function is the characterization of the sag potential(17). This hallmark of I_h activation is measured as the amount of rectification detected in response to hyperpolarizing current injections. In line with previous reports,

101 we found that L2/3 PCs exhibited an unremarkable amount of sag potential at 'typical' current
102 commands. However, upon larger negative current injections, a discernable rectification was revealed
103 (Fig. 2a). In addition, the rectification of the steady-state responses was abolished in the presence of
104 external Cs^+ which could be restored by artificial I_h supplementation by dynamic clamp (Fig. 2b).
105 Similarly, sag was non-detectable when I_h was blocked, which could then be restored by dynamic
106 clamp (Fig. 2c,d). Furthermore, we found that passive electrical properties were also significantly
107 modulated by HCN blockade (Fig. 2e,f). Together, these results explain the dramatic effect of Cs^+ on
108 excitability (Fig. 1). The non-apparent sag potential at conventional hyperpolarizing current steps is
109 thus surprising, suggesting a markedly faster occurrence of the I_h effect exists in L2/3 PCs which
110 occludes the biphasic nature of the sag response. To investigate this possibility, we measured the time-
111 constant of the immediate voltage responses. We found a strong positive correlation between the
112 amplitude of a passive current command and the voltage response time constant, which was abolished
113 by Cs^+ bath application (Fig. 2g). This confirms that I_h has a strong effect during the initial phase of
114 hyperpolarizing voltage responses which may contribute to the lack of detectable sag potential at
115 modest current injections. However, other biophysical mechanisms may also contribute to the muted
116 sag effect in L2/3 PCs.

117 Next, we examined the voltage dependence and kinetic properties of I_h in L2/3 PCs in voltage clamp
118 (Fig. 2h). Significant Cs^+-sensitive (1mM) currents were activated at subthreshold membrane
119 potentials, with half-activation voltages more negative than the resting membrane potential, and with
120 relatively fast activation kinetics (Fig. 2i,j). Overall the pharmacological profile, effects on passive
121 electrical properties, and voltage dependence all point to previously published data describing HCN
122 channels (24). Together these results indicate that L2/3 PCs express a functionally relevant population
123 of HCN channels, which constrain the excitability of these cells. Similar voltage clamp responses were
124 observed beyond the visual cortex (e.g., in S1, M1, and A1; Supplementary Fig. 1) suggesting that
125 HCN channels are a consistent feature in L2/3 PCs across sensory cortices.

126

127 **Noncanonical subthreshold signal processing in L2/3 PCs by I_h**

128 Electrical signals at different dendritic compartments undergo distance-dependent distortion (22, 25),
129 which has a major effect on neuronal function in cells with extensive dendritic branching (26). To
130 counteract these effects, larger L5 PCs and CA1 PCs express HCN channels with nonuniform
131 distributions (18, 24). As L2/3 PCs have a much more compact morphology, synaptic input distortions

132 might be less severe, raising the possibility of an alternative function of HCN channels in these cells.
133 Thus, to investigate the distance-dependence of HCN on L2/3 synaptic inputs we made whole-cell
134 patch recordings from Alexa-594 filled L2/3 PCs, and performed extracellular minimal stimulation at
135 different dendritic locations guided with 2P microscopy (Fig. 3a). Elicited EPSPs likely reflect the
136 activation of a single axon as stimulus intensity was set to achieve an ~50% failure rate(27). As HCN
137 deactivation has been shown to strongly impact the duration of synaptic events(22, 25), we quantified
138 changes in the half-width of locally evoked EPSPs, here using the HCN-selective blocker ZD-7288
139 (50 μM). Surprisingly, our results were in contrast to previous reports in L5 and CA1 PCs, in that I_h
140 block had a far smaller effect on the time-course of distally-evoked (>100 μm distance from the soma)
141 synaptic responses. In contrast, proximal inputs (<100 μm) were markedly more broadened after I_h
142 blockade (Fig. 3b,c). These results suggest that L2/3 PCs are equipped with a distinctive subcellular
143 HCN distribution, potentially contributing to noncanonical distance-dependent input modulation along
144 the dendritic axis of L2/3 cells.

145

146 **Pathway-specific modulation of synaptic information**

147 L2/3 PCs receive information from distinct brain regions, such as "top-down" (cortical-cortical) axons,
148 generally arriving to layer 1(28) and "bottom-up" (thalamocortical/layer 4) axons, terminating on
149 proximal dendrites located in layer 4 and 2/3(29). Due to the stronger proximal effect of HCN on L2/3
150 PC EPSPs, we explored whether this modulation yielded input-pathway-specific differences. Whole-
151 cell recordings were again obtained from L2/3 PCs, and EPSPs were elicited by minimal stimulation
152 with electrodes situated to preferentially stimulate either layer 4 or layer 1 axons (electrode placement
153 ~200μm laterally from recorded PC in either layer). In a subset of our recordings stimulating layer 4
154 inputs, evoked EPSPs were substantially larger than spontaneously occurring events (Fig. 3d). We
155 deemed these as inputs arriving directly from the lateral geniculate nucleus axons (putative direct
156 thalamocortical input(30) from the LGN, Supplementary Figure 2.). I_h blockade significantly
157 broadened elicited EPSPs when the stimulation electrode was placed in layer 4, but not in layer 1 (Fig.
158 3e). Consequently, the voltage integral of EPSPs was significantly larger for L4 inputs compared to
159 those in L1 (Fig. 3f). The effect of Cs^+ on EPSP half-width and voltage integral was similar for both
160 L4 and putative LGN inputs, suggesting intermingled termination zones(29). Together these results
161 suggest that HCN channels preferentially regulate bottom-up nonlinear signaling in proximal dendritic
162 regions in L2/3 PCs.

163 HCN channels are notable for their ability to restrain temporal integration of synaptic inputs(22).
164 Therefore, we repeated these experiments using more high-frequency stimulation (5 stimuli at 50 Hz;
165 Fig. 3g). In accordance with the effect on single EPSPs, summation of L1 (i.e., 'distal) inputs was
166 unaltered with HCN block. In contrast, HCN blockade led to increased temporal summation of L4
167 inputs (Fig. 3h,i). However, summation of putative LGN inputs was not affected by HCN channel
168 block, suggesting further diversification of active properties even between L4 and LGN inputs as well.

169

170 **I_h channels constrain NMDA receptor-dependent synaptic boosting**

171 In a passive environment, dendritic filtering (31) creates attenuated (i.e., wider) EPSPs when
172 originating further from the soma. Yet our results show an opposite phenomenon with HCN channels
173 blocked. It has been described that reduced HCN availability can facilitate dendritic boosting
174 mechanisms, via activation of either voltage-gated (32) or NDMA (33) channels. To investigate
175 possible contributions of dendritic voltage-dependent processes, we performed NEURON
176 computational simulations using a realistic L2/3 PC dendritic morphology (34). Inserting voltage-gated
177 sodium or potassium channels with various distributions could not recapitulate our distance-dependent
178 EPSP observations (Supplementary Figure 3.). Thus, we next investigated whether NMDA receptors
179 might play a role in the observed phenomenon, due to their described overwhelming contribution to *in*
180 *vivo* activity in L2/3 PCs (8, 35).

181 We first tested whether NMDA receptors contribute to spontaneously occurring synaptic inputs
182 (sEPSPs) in L2/3 PCs(36). Due to potential alterations in spontaneous release and overall circuit
183 activity, extracellularly applied NMDA blockers may introduce significant confounds for this line of
184 investigation, especially as spontaneous synaptic potentials show tremendous variability in frequency,
185 amplitude, and kinetics. To overcome this conundrum, we designed a custom-built pipette attachment
186 through which the intracellular solution could be stably exchanged during whole-cell recordings (37).
187 We recorded sEPSPs in L2/3 PCs first using control intracellular solution, which was then exchanged
188 to a 50 μM MK-801 (non-competitive NMDA receptor antagonist) containing intracellular solution
189 (Fig. 4a). To also capitalize on the voltage-sensitivity of NMDA receptors, average peak amplitudes
190 were recorded at two different membrane potentials for each intracellular condition; -80 mV and -55
191 mV (resting membrane potential, and a somatic membrane potential depolarized enough to partially
192 unblock NMDA receptors (38)). Due to the small nature of sEPSPs, quantification of other waveform
193 parameters (i.e., EPSP width) was avoided. After quantifying the mean sEPSP peak at -80 mV, we

194 calculated the expected (linear) sEPSP peak at -55 mV and compared this prediction to our
195 observations of -55 mV. We found that sEPSPs were significantly larger than predicted after
196 depolarization (Fig. 4b), alluding to the presence of a nonlinear boosting mechanism. We found that
197 intracellular MK-801 solution exchange could abolish this synaptic amplification (Fig. 4c), indicating
198 that NMDA receptors actively contribute to shaping naturally occurring sEPSPs in L2/3 PCs. The
199 effect of pipette perfusion itself on our measurements was negligible (Supplementary Figure 4)

200 Having established that NMDA receptors play an active role in modulating sEPSPs, we next explored
201 whether differential NMDA recruitment could explain the observed boosting of proximal synaptic
202 inputs following HCN blockade described earlier. Computational simulations (lacking HCN) (Fig. 4d)
203 revealed that a proximally-biased NMDA distribution, as seen in other PC types (39), could indeed
204 recapitulate our experimental findings in L2/3 PCs with high accuracy (Fig. 4e,f). Because HCN
205 channels can reduce NMDA recruitment during synaptic signaling, we next explored whether proximal
206 enrichment of HCN allows for bottom-up-specific gating of NMDA (Fig. 4g). To accomplish this, we
207 recorded L2/3 EPSPs following stimulation of both proximal L4 and distal L1 inputs, as described
208 earlier, during each recording and varied the background pharmacology. Intriguingly, L4-evoked
209 EPSPs were slightly narrower than L1 in control conditions, potentially owing to increased HCN in
210 proximal dendrites. This layer-specific relationship was inverted following extracellular Cs^+ to block
211 HCN (Fig. 4g,h). To confirm that this L4-specific EPSP broadening after HCN channel block was due
212 to NMDA-inducted boosting, as predicted in our simulations (Fig. 4f), we next examined the EPSPs
213 with Cs^+ and MK-801 together. In the presence of internal MK-801, the broadening effect of Cs^+ on
214 L4-evoked EPSPs was abolished, thereby reverting the L4-L1 EPSP relationship to a control-like state.
215 (Fig. 4g,h). Together, our modeling and experimental results indicate that NMDA-directed
216 amplification of L4 inputs is strongly constrained by a proximal HCN bias in L2/3 PCs dendrites,
217 allowing for pathway-specific modulation of 'bottom-up' inputs without affecting those arriving from
218 'top-down' L1 axons.

219

220 **Noncanonical HCN distribution predicted in L2/3 PCs**

221 We next carried out computational simulations for HCN in L2/3 PCs, based on our previous
222 observations and modeling. To reproduce the native relationship between EPSP halfwidth and
223 dendritic distance, HCN channels were inserted into the model with different distributions and
224 conductance densities (Fig 5a). Our simulations revealed that proximal bias in HCN channel

225 distributions could best recapitulate our observations of HCN on proximally and distally originating
226 EPSP halfwidths. providing the best fit to our measurements (Fig. 5b,c). According to these
227 simulations, HCN regulation of local input resistance constrained voltage-dependent NMDA receptor
228 activation. This is in line with the proximal HCN1 channel staining (Fig. 1) revealed by
229 immunohistochemistry. These results suggest that L2/3 PCs have a unique proximal HCN channel
230 bias, as previous experiments show a distal HCN expression in L5 PCs and CA1 PCs(18, 24). Possibly
231 due to the markedly different morphology, specifically the absence of an independent computational
232 tuft unit, HCN channels have different functions in L2/3 PCs. Thus, together with experimental
233 observations, these simulations indicate that HCN channels are well positioned to regulate bottom-up
234 proximal inputs in L2/3 PCs, contrary to their L5 PC counterparts, which express HCN distally to
235 counteract distance dependent passive filtering from top-down inputs.

236

237 **Tight developmental upregulation of Layer 2/3 HCN channels**

238 Several ion channels show postnatal maturation in their biophysical properties and surface
239 expression(40), raising the possibility of a different proximo-distal HCN bias in young L2/3 PCs
240 compared to adult animals. To examine this possibility, L2/3 PCs were recorded at three developmental
241 time points (1st, 2nd and 6th postnatal week) in S1. Our initial assessment of HCN maturation showed
242 that a rapid developmental upregulation occurs between 1 and 2 weeks old. We opted to perform further
243 developmental experiments in primary somatosensory cortex, where cells already receive adequate
244 bottom-up information during the first and second postnatal week.

245 We found that 1 week old L2/3 PCs displayed markedly different passive properties, while 2-week-
246 old cells were quite similar to mature cells (Fig. 6a). The non-quantifiable sag potential in 1 week old
247 animals implies the lack of I_h current at this developmental time point, however, the disproportionately
248 large input resistance and elevated resting membrane potential also suggests that other background
249 leak channels may also be missing at this developmental window (Fig. 6b). Subsequent voltage clamp
250 recordings confirmed that L2/3 PCs in 1 week old animals do not possess a considerable amount of I_h
251 in contrast to 2 and 6 week old animals (Fig. 6c,d). We found that both resting membrane potential and
252 peak I_h conductance changes throughout development were tightly (negatively) correlated (Fig. 6e).
253 This provides additional evidence for parallel maturation of HCN with other leaky channels, as HCN
254 channel expression alone would be predicted to shift the membrane to more depolarized potentials
255 (Fig. 2e). Next, we mapped the distance-dependence dendritic EPSP kinetics in 1 week old animals

256 (Fig. 6f). We found a surprising 'non-Rallian' negative correlation between EPSP halfwidth and
257 stimulation distance from the soma (Fig. 6g, h), similar to our previous results from mature neurons
258 with HCN channels blocked (Fig. 3a,b). This suggests the presence of nonlinear boosting mechanisms
259 in proximal dendrites of developing L2/3 PCs, similar to mature cells, which are unabated due to the
260 lack of HCN at this developmental stage.

261

262 **I_h dependent neuromodulation of L2/3 PC activity by serotonergic inputs**

263 If the robust dendritic HCN availability in mature L2/3 PCs is unalterable, the ability of NMDA to
264 modulate bottom-up inputs might be inadequate. Whether the mature brain possesses mechanisms to
265 modulate HCN in L2/3 PCs is unknown. Nonetheless, previous work in cortical L5 PCs shows that I_h
266 currents can be modulated following 5-HT_7 serotonergic receptor activation(41). L2/3 PCs are
267 extensively innervated by serotonergic axons from the dorsal raphe (42), providing a potential
268 framework to modify HCN availability. Single-cell RNA-seq (23) showed that L2/3 PCs do express
269 5-HT_7 receptors, interestingly at higher levels than all other cortical PCs (Fig. 7a). We
270 pharmacologically evaluated a potential role of serotonergic HCN regulation by bath application of 5-
271 carboxamidotryptamine (5-CT; 30 nM), a specific 5-HT_7 agonist. 5-CT application significantly
272 reduced evoked firing of L2/3 PCs during extracellular stimulation in L4 (Fig. 7b). Current clamp
273 experiments revealed that the rectification of steady-state voltage responses to hyperpolarizing current
274 injection was amplified with 5-CT (Fig. 7c), likely due to the increased availability of HCN channels
275 due to a rightward shift in their activation voltage-dependence (Fig. 7d). 5-CT also reduced L2/3 input
276 resistance potentially via HCN regulation, however, did not yield a depolarizing effect on the resting
277 membrane potential nor affect AP threshold (Fig. 7e). Importantly, 5-CT had no impact on the firing
278 responses of L2/3 PCs when I_h currents were blocked with background Cs^+ throughout the experiment
279 (Fig. 7f). Furthermore, the dampening of neuronal output was not related to an downregulating effect
280 of 5-HT7 on NMDA receptors (Fig. 7g, (43)). Together these results indicate that neuromodulation
281 represents an endogenous mechanism by which HCN availability can be altered in L2/3 PCs.

282

283 **DISCUSSION**

284

285 Precise communication between cortical neurons relies on discrete pre- and postsynaptic forms of
286 information transfer at synapses. The majority of cortical synapses terminate along the dendritic tree

287 (44) where, based on local active and passive electrical properties, various types of nonlinear
288 transformations occur. The spatially and electrically disjointed nature of dendrites (45) from the rest
289 of the cell allows for local, soma-independent computation. For example, perturbing active dendritic
290 elements (i.e., local conductances) can impair several fundamental cortical circuit tasks (36) such as
291 perception (14), underlining the necessity for compartmentalized information processing. Further,
292 single-subunit model simulations are unable to reproduce *in vivo* observed activity patterns of L2/3
293 PCs(9). Here, by combining *ex vivo* current clamp, synaptic stimulation, and ion channel recordings
294 with empirically informed, biophysically realistic simulations, we demonstrate that L2/3 PCs in
295 sensory cortex express a previously unappreciated, proximally-biased HCN channel distribution. Due
296 to an apparent universal HCN expression in L2/3 cells from each region, this arrangement should allow
297 for modification of synaptic gain across all primary sensory areas of cortex. One of the basic functions
298 of L2/3 PCs in sensory cortex is to encode first-order information, such as the orientation of visual
299 input(2, 46, 47). Several investigations propose that arithmetic summation of a number of similarly
300 tuned synapses will dictate whether these neurons will fire in response to sensory input (48). However,
301 numerous dendritic nonlinearities have been established in L2/3 PCs, such as NMDA receptors (8)
302 sodium channels (11) and calcium channels (10, 49) which also contribute to this process. Here we
303 demonstrate that L2/3 PCs express a functionally relevant population of HCN channels well situated
304 to modify the gain of cortical sensory and contextual information processing.

305 We found that HCN channels in L2/3 could constrain fundamental aspects of cellular
306 excitability, such as input resistance and resting membrane potential. This is likely due to a strong
307 proximal somato-dendritic distribution of HCN channels, as observed in immunohistochemical
308 experiments here. Likely due to their influence on input resistance, HCN blockade resulted in greatly
309 increased AP firing during extracellular stimulation. L2/3 HCN channels strongly dampened excitatory
310 synaptic inputs, however, only to those arriving at proximal dendritic locations. In line with this result,
311 HCN channels reduced the timecourse of synaptic inputs following local stimulation in L4, but left
312 those following L1 stimulation unaffected. Together with additional input-specific pharmacological
313 experiments, NEURON simulations demonstrated that this input-specific synaptic phenomenon could
314 indeed be explained by a proximal HCN channel distribution in dendrites putatively situated in L4 and
315 L2/3. This was apparently only possible with a concurrent proximal NMDA recruitment bias. This
316 should not be confused with observed differences in NMDA recruitment along the axis of individual
317 L2/3 basal dendrites (36). Although a proximal-basal dendrite NMDA receptor distribution is in line
318 with findings from L5 PCs (50), HCN channels are instead enriched distal dendritic compartments in
319 these PC types (18, 24). Thus the unprecedented proximal HCN recruitment in L2/3 PCs permits

320 pathway-specific control of synaptic amplification, as bottom-up (i.e., L4 originating) inputs target
321 proximal dendritic compartments homogeneously (29). This was in opposition to top-down inputs,
322 whose axons largely target distal dendrites in L2/3 PCs (28, 51), as these synapses were unaffected by
323 HCN channel blockade. To fully understand how compartment-specific pathways are functionally
324 regulated, further anatomical and *in vivo* imaging experiments are needed to establish the distribution
325 and synaptic dynamics of L4 and L1 inputs along the L2/3 PC dendritic tree.

326 HCN channels appear well suited to regulate the synaptic and intrinsic properties of L2/3 PCs,
327 for example, if their availability is plastic or developmentally regulated. Previously, we found that
328 HCN channel availability was upregulated in GABAergic interneurons during development, resulting
329 in reduced propagation of subthreshold signals in mature axons (52). Interestingly, we found that L2/3
330 PCs in young animals (1 week old) lacked HCN channels. Together, these results suggest a universal,
331 cell-nonautonomous developmental HCN upregulation in both dendritic and axonal compartments. In
332 L2/3 PCs, the HCN channel maturation window was rapid and almost complete by the second postnatal
333 week. Therefore critical period plasticity (53) and developmental I_h upregulation occur during a similar
334 developmental window, suggesting a causal relationship. In addition to the robust developmental
335 regulation of HCN channels, we also found that enhancement of HCN channel availability was also
336 possible in the adult cortex, following serotonergic (5-HT_7) receptor-mediated biophysical regulation.
337 This was likely due to a metabotropic process that increases cytosolic cAMP levels by stimulating
338 adenylate cyclase(54) which in turn modulates HCN channel properties. This raises the intriguing
339 possibility that neuromodulation could induce nonstationary conditions in mature L2/3 circuits, for
340 example, in re-biasing of bottom-up vs. top-down information, experience-dependent plasticity (55),
341 or even for reopening of critical window-like states (56).

342 As L2/3 PCs are one of the most abundant cell populations of the neocortex, HCN channels in
343 these cells may exert overwhelming control over cortical excitability and thus cognition and memory.
344 Cell non-autonomous HCN channel dysregulation manifests in clear behavioral changes, such as
345 altered spatial learning (57) or impaired working memory (58). Curiously, higher HCN1 protein levels
346 in the postmortem brain also correlate with cognitive resilience in aging humans (59). Therapeutic
347 HCN channel modulation aimed at restoring healthy brain function in distinct pathophysiological states
348 has consequently garnered significant interest (60-62) as both HCN1 and HCN2 are linked to
349 neuropathic pain (63) and for treating major depressive disorder (61, 62, 64). Here we demonstrate that
350 activation of the serotonergic receptor 5-HT_7 alters HCN channel function in L2/3 PCs, resulting in
351 reduced PC excitability, similar to L5 PCs (41). 5-HT_7 receptor targeting agents are highly effective
352 psychopharmacological compounds. Agents such as the antidepressant *vortioxetine* has a relevant

353 therapeutic concentration that functionally suppresses 5-HT_7 (65), and the mood-stabilizing
354 antipsychotic agent *lurasidone* possesses an even higher binding affinity to 5-HT_7 (66). Commonly
355 used anesthetic drugs also modulate HCN channel action (67, 68), implying the need to investigate
356 anesthesia-related mechanisms and confounds in L2/3 in both therapeutic and experimental settings.
357 Together, we argue that HCN channels are present and functionally relevant in L2/3 PCs. As L2/3 PCs
358 are one of the largest cell populations in the brain, and as HCN channels are the target of several current
359 therapeutics, future research should consider their role in these cells in basic and clinical studies.
360

361 **METHODS**

362

363 **Acute slice preparation**

364 All animal procedures were approved by the Emory University IACUC. Acute slices from cortex were
365 prepared from mature C57Bl/6J mice (6–10 weeks old). Male and female mice were used for all
366 experiments with data collected from ≥3 mice per experimental condition. Mice were first anesthetized
367 and perfused with ice-cold cutting solution (in mM) 87 NaCl, 25 $NaHO_3$, 2.5 KCl, 1.25 NaH_2PO_4, 7
368 $MgCl_2$, 0.5 $CaCl_2$, 10 glucose, and 7 sucrose. Thereafter, mice were terminated by decapitation and the
369 brain immediately removed by dissection. Brain slices (250 µm) were sectioned in the coronal plane
370 using a vibrating blade microtome (VT1200S, Leica Biosystems) in the same solution. Slices were
371 transferred to an incubation chamber and maintained at 34°C for ~30 min and then at 23–24°C
372 thereafter. During whole-cell recordings, slices were continuously perfused with (in mM) 128 NaCl,
373 26.2 $NaHO_3$, 2.5 KCl, 1 NaH_2PO_4, 1.5 $CaCl_2$, 1.5$MgCl_2$, and 11 glucose, maintained at 30.0°C ± 0.5°C.
374 All solutions were equilibrated and maintained with carbogen gas (95% O_2/5% CO_2) throughout.

375 **Electrophysiology**

376 L2/3 PCs were targeted for somatic whole-cell recording in the layer 2/3 region of primary visual
377 cortex by gradient-contrast video microscopy. Electrophysiological recordings were obtained using
378 Multiclamp 700B amplifiers (Molecular Devices). Signals were filtered at 6–10 kHz and sampled at
379 50 kHz with the Digidata 1440B digitizer (Molecular Devices). For whole-cell recordings, borosilicate
380 patch pipettes were filled with an intracellular solution containing (in mM) 124 potassium gluconate,
381 2 KCl, 9 HEPES, 4 $MgCl_2$, 4 NaATP, 3 l-ascorbic acid, and 0.5 NaGTP. Pipette capacitance was

382 neutralized in all recordings and electrode series resistance was compensated using bridge balance in
383 current clamp. Liquid junction potentials were uncorrected.

384 For cell attached recordings seal resistance of >1GΩ was established, for accurate measurement of
385 action potentials. A stimulating electrode was placed in either layer 4 or layer 1 region of the visual
386 cortex, at least 200 µm away from the recorded soma. Stimulation intensities were calibrated to reliably
387 elicit at least 3, but no more than 10 action potentials during the 20 consequent stimuli (50 Hz, 30 s
388 inter-trace intervals, 10-50 µs stimulus length). Stability of the elicited responses was confirmed by an
389 initial 15 repeated measurements. Recordings were post hoc filtered at 2 kHz to remove stimulation
390 artifacts.

391 Recordings had a series resistance <20 MΩ. Membrane potentials were maintained near –80 mV during
392 current-clamp recordings using constant current bias. AP trains were initiated by somatic current
393 injection (300 ms) normalized to the cellular capacitance in each recording measured immediately in
394 voltage clamp after breakthrough (69). Cellular electrical and firing parameters were established by
395 recording voltage responses to current steps between -6 pA/pF and 20 pA/pF. Input resistance was
396 measured by averaging voltage responses to a 20 pA prepulse current step. Sag ratio was determined
397 as the ratio between the sag amplitude and the steady-state response during increasing -2 pA/pF current
398 steps.

399 To establish distance dependent EPSP kinetics, cells were filled with 10 µM Alexa-594. Dendrites
400 were visualized after cell fill with Alexa 594 (10µM) with two-photon laser scanning microscopy using
401 a commercial scan head (Ultima; Bruker Corp) fitted with galvanometer mirrors using a 60x, 1.0 NA
402 objective. The fluorophore was allowed to equilibrate for at least 10 minutes before imaging. The
403 stimulating electrode, filled with extracellular recording solution, was placed in close proximity (<5
404 µm) of the two-photon visualized dendrite. Stimulation intensity was calibrated to elicit an EPSP with
405 <1 ms delay and approximately 50% failure rate (54.21 ± 8.72%, n= 41). The 50% failure rate was
406 necessary in order to maximize the possibility of stimulating a single input. For layer 1, layer 4, and
407 putative LGN input stimulations the procedure was the same. Synaptic summation was probed by
408 eliciting 5 consequent responses at 50 Hz. Stimulation intensity was elevated during these recordings
409 to elicit synaptic responses every time for the first stimuli as failures introduced by lower stimulation
410 intensities can yield inconsistent input activation during the 5 stimuli.

411 For voltage-clamp recordings, cells were patched in normal extracellular solution to first record their
412 firing patterns. Voltage protocols for I_h current measurements consisted of 300 or 500 ms long voltage
413 steps between −150 and −60 mV. Activation time constant was measured by fitting the initial 100 ms
414 of the current response with a single exponential function. In a subset of recordings CsMeSO4 (2 mM)
415 was bath applied after recording control current responses, to establish cesium-sensitive I_h current
416 kinetics and voltage dependence by subtraction. Series resistances were between 6–20 MΩ (75–80%
417 compensated with 53 µs lag) and were constantly monitored. Data were discarded if the series
418 resistance changed more than 25%.

419 The dynamic clamp system was built in-house based on a previous publication(70), related online
420 available materials available here: (http://www.dynamicclamp.com/). The equations governing the
421 implemented gHCN were identical to those used in the NEURON model construction. Synaptic
422 conductances were built-in predefined conductances available from http://www.dynamicclamp.com/.

423 **Intracellular solution perfusion**

424 Intracellular solution was perfused by a custom-built tubing and relay system attached to the pipette
425 holder. Briefly, the pipette was filled with normal intracellular solutions to measure firing patterns and
426 subsequent control measurements of spontaneous and elicited EPSPs. Next, a second intracellular
427 solution was introduced to the pipette through a small tube drilled through the pipette holder, by
428 applying miniscule positive pressure. The intracellular fluid levels were marked before the recording
429 and through a second tube the intracellular solution was siphoned out, to not alter established pipette
430 capacitance. During initial trial experiments using fluorophores in the second intracellular solution it
431 was determined that two minutes is enough for complete exchange of the intracellular solution and
432 intracellular equilibration as well. Data were discarded if the series resistance or pipette capacitance
433 changed more than 20%.

434 **Immunohistochemistry**

435 Two-month-old mice were anesthetized with Nembutal (50mg/mL, i.p.) and perfused transcardially
436 with 4% paraformaldehyde (PFA), 0.05% glutaraldehyde in phosphate buffered saline (PBS). After
437 perfusion, brains were removed from the skull and immersed in 4% PFA overnight at 4°C. Coronal
438 100 µm-thick sections were then cut on a Vibratome (Leica V1000). Brain slices were permeabilized
439 and incubated in blocking buffer for one hour at room temperature. After blocking, sections were

overlaid with primary antibody to HCN1 (1:200, Thermo Fisher Scientific) overnight at 4 °C, then subjected to a 1 h incubation with secondary antibody (Goat anti-Rabbit IgG, 1:200, Thermo Fisher Scientific) at room temperature. Stained sections were mounted with DAPI-containing mounting solution and sealed with glass coverslips. Confocal imaging was carried out on a Leica SP5 MP.

NEURON modeling

Computer simulations were performed using the NEURON simulation environment (versions 7.5 and 7.6, downloaded from http://neuron.yale.edu). A constrained NEURON model with an active somatic compartment was downloaded from the publicly available Cell Type Database of the Allen Institute (http://celltypes.brain-map.org/experiment/electrophysiology/487661754). Passive properties (axial resistance, specific membrane capacitance and leak conductance density) were altered to recreate passive membrane potential responses of whole-cell recorded L2/3 PCs for given stimulus intensities. Both transient and persistent potassium channels were taken out of the model to gain simulation speed as the aim of the simulations was to reproduce subthreshold EPSP dynamics. Final simulations were rerun with intact sodium currents as well to confirm the lack of alterations introduced by these channels. The I_h conductance was based on the built-in Hodgkin–Huxley model of NEURON with freely adjustable sets of parameters(71). I_h model parameters were constrained by our whole-cell voltage clamp recordings. The steady-state activation was governed by the following equation:

$$minf = \frac{1}{1 + e^{\frac{v+21.945}{6.85}}}$$

where v is the local membrane potential. Due to the lack of apparent inactivation, the model operated with a single gate (activation).

The activation and deactivation time constant was defined as

$$mtau = 25.46 * e^{-0.5*\left(\frac{v+100.28}{16.2}\right)^2}$$

To simulate EPSP kinetics, a movable spine (length: 0.6 µm, diameter: 0.6 µm, axial resistance: 150 Ωcm), with spine neck (length: 2 µm, diameter: 0.1 µm, axial resistance: 100 Ωcm) was created. Leak conductance was inserted into both compartments, along with the fitted conductance model. Synaptic inputs were supplemented by using NEURON's built-in AlphaSynapse class. To probe the contribution

466 of specific dendritic conductances to shaping the distance-EPSP halfwidth relationship, selected
467 conductance models were inserted into both apical and basal dendrites with a Gaussian distribution.
468 This curve was selected as modulation of the Gaussian curve's width and y-offset can reproduce a wide
469 variety of feasible distributions such as linear, exponential, or hot-zone-like expression. To model the
470 contribution of dendritic sodium, potassium, and calcium channels to input modulation, NaTs, Kv3_1
471 and Ca_LVA models were selected. Distribution approximation was done by grid search to avoid local
472 fitting minimums. NMDA receptors were implemented based on a previous publication (72). During
473 the fitting procedure, NMDA activation voltage and AMPA:NMDA ratios were adjusted.

474 **Statistics**

475 Averages of multiple measurements are presented as mean ± SD. Data were statistically analyzed by
476 ANOVA test using Origin software and custom-written Python scripts. Normality of the data was
477 analyzed with Shapira-Wilks test.
478

479 **Data and software availability**

480 All code used for simulating single and multicompartmental NEURON models will be made available
481 on Github and public repositories.
482
483
484
485
486
487
488
489
490
491
492
493

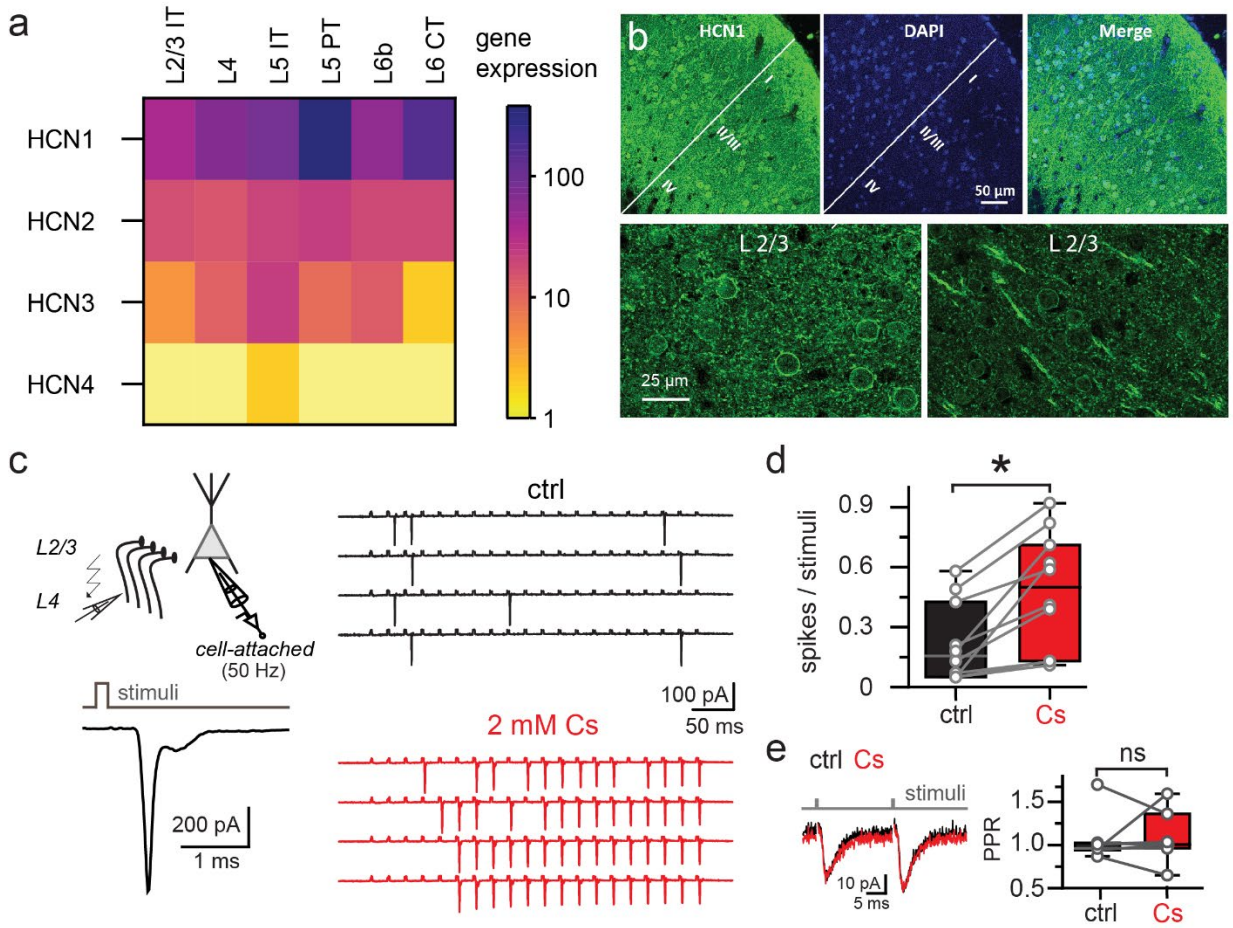

Fig 1. HCN expression and effect of Cs^+ on AP firing in cortical L2/3 PCs

a. HCN gene subunits show uniform expression pattern among cortical PC types. Data is collected from the online available dataset(23). **b.** HCN1 immunohistochemistry reveals dense somatic expression in layer 2/3 of the visual cortex **c.** HCN channels control the excitability of L2/3 PCs. Schematic illustration of the experimental arrangement of cell attached recordings during extracellular stimulation of L4, and the shape of the elicited action potential (left). Increased spiking of L2/3 PC upon blockade of HCN channels with 2 mM CsMeSO4 (right). **d.** Pharmacological block of I_h significantly increases the firing response of L2/3 PCs (0.22 ± 0.06 Hz vs. 0.48 ± 0.09 Hz for control vs CsMeSO4 bath application, p=0.002, t(9)=-4.42, Student's paired t-test, n=10. **e.** Presynaptic contributions were examined using the paired-pulse ratio (PPR) in whole cell current clamp recordings (1.09 ± 0.12 Hz vs. 1.17 ± 0.15 Hz for control vs CsMeSO4 bath application, p=0.422, t(6)=-0.8612, Student's paired t-test, n=7).

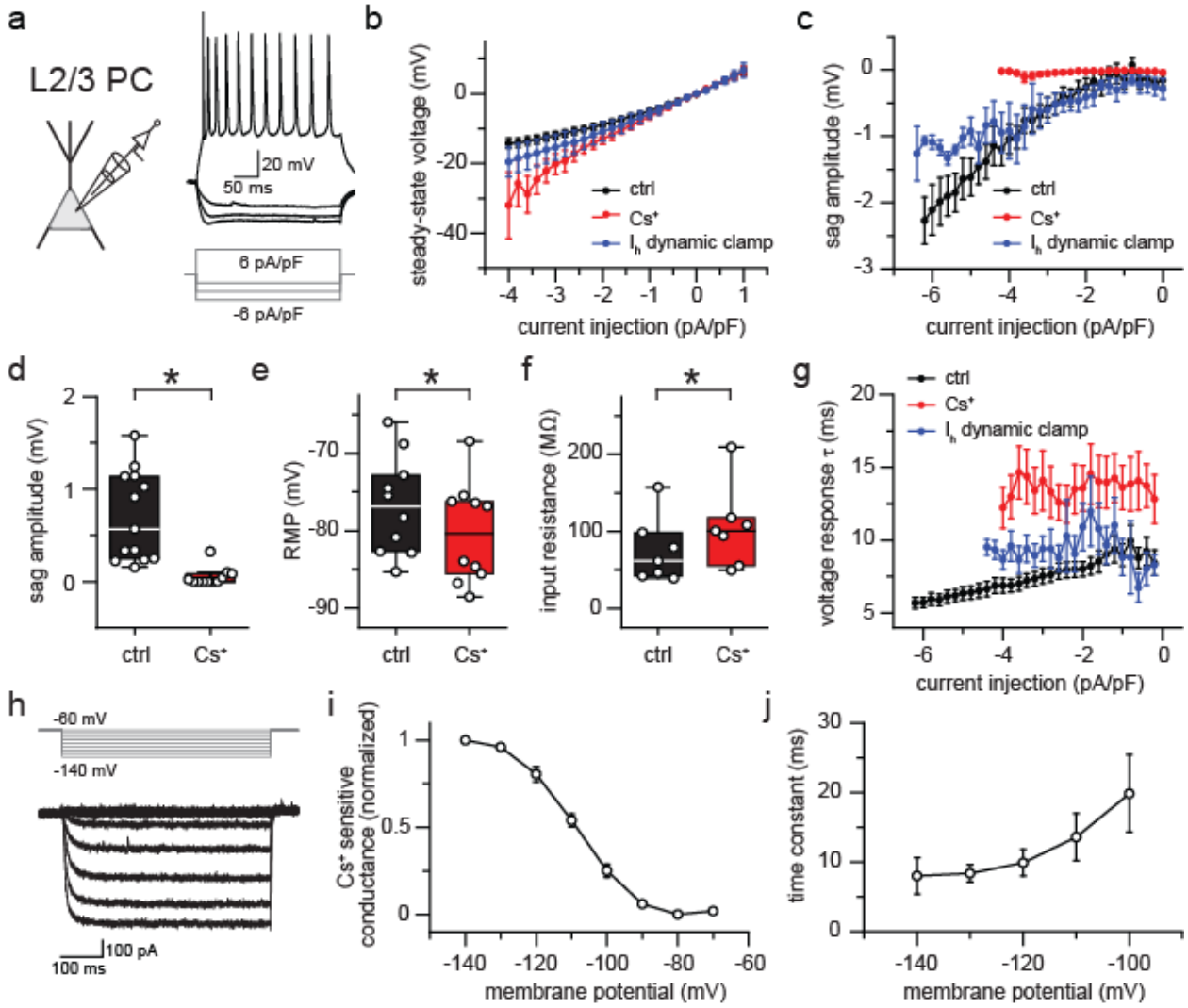

Fig 2. Functionally relevant I_h in L2/3 PCs

a. Whole cell current clamp recordings showing sag response to very negative current commands. **b.** Steady-state voltage response rectification upon hyperpolarizing current injections is mediated by I_h. **c.** Sag voltage is abolished by blocking I_h. **d.** Sag amplitude is Cs^+ sensitive (0.7 ± 0.49 mV vs. 0.05 ± 0.1 mV for control vs CsMeSO4 application, $p=2.46^{-4}$, t(22)=4.37, Student's two-sample t-test, n=13 and 11). **e.** Resting membrane potential is modulated by I_h (-76.75 ± 6.37 mV vs. -80.29 ± 6.48 mV for control vs CsMeSO4 bath application, $p=1.98^{-4}$, t(9)=6.02, Student's paired t-test, n=10). **f.** Input resistance is altered by I_h (74.78 ± 42.34 mV vs. 104.99 ± 52.91 mV for control vs CsMeSO4 bath application, p=0.048, t(6)=-2.48, Student's paired t-test, n=7). **g.** The time course of voltage responses to hyperpolarizing current on the magnitude of the current injection is abolished by Cs^+. **h.** Example voltage clamp recording of cesium sensitive currents in a L2/3 PC. **i.** Voltage dependence of cesium sensitive current activation, **j.** Voltage dependent activation kinetics of cesium sensitive currents.

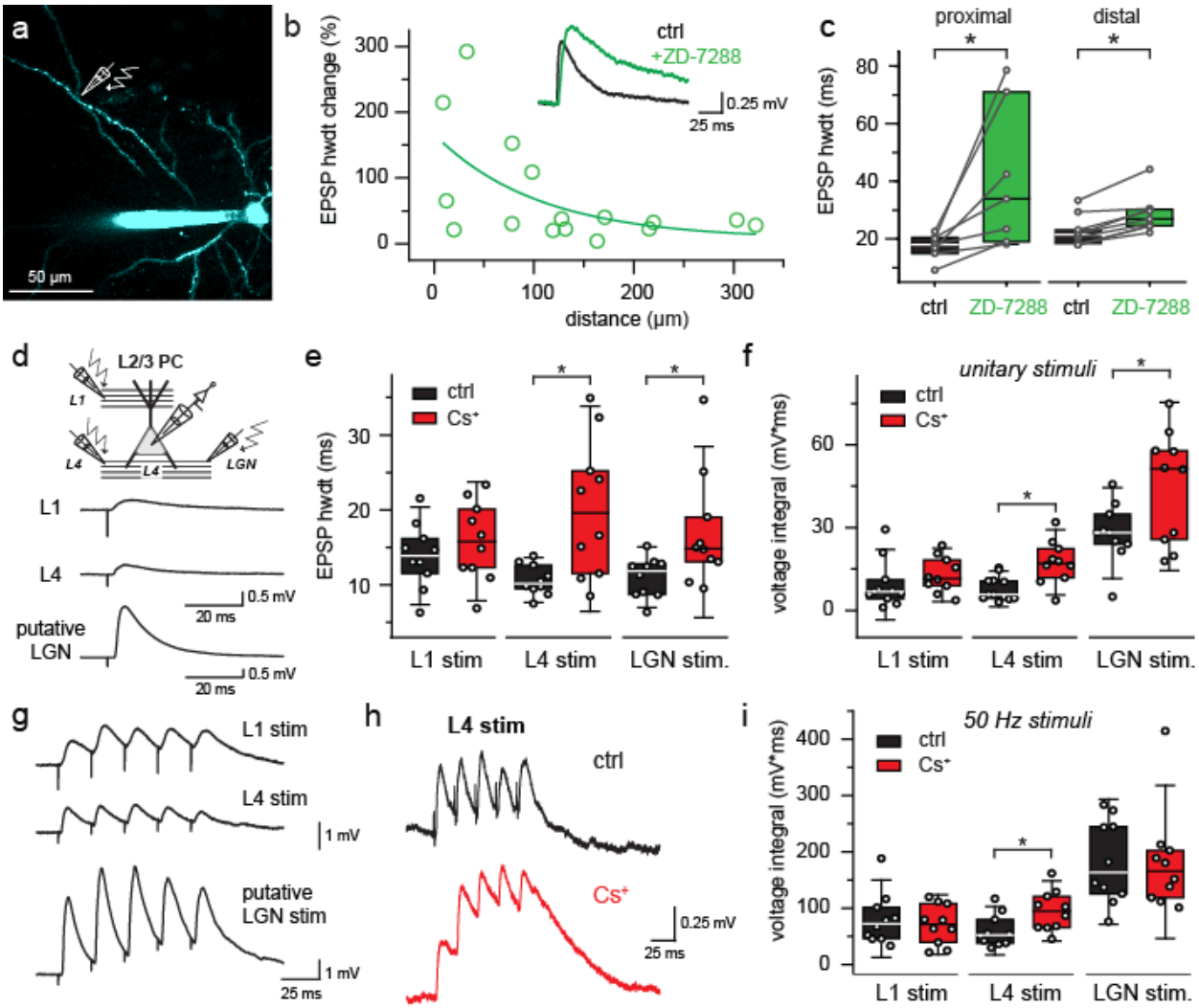

Fig 3. Noncanonical effect of I_h block on EPSPs in L2/3 PCs

a. Experimental arrangement of extracellular targeted stimulation of a L2/3 PC dendrite. **b.** Application of ZD-7288 revealed a proximal bias for EPSP modulation by I_h (Exponential fit τ=104.7 µm, R^2=0.33, n=18). **c.** EPSP halfwidth is significantly modulated along the dendritic axis by I_h, (proximal dendritic locations: 17.42 ± 1.68 ms vs. 40.95 ± 24.78 ms for control vs 50µm ZD-7288 bath application, p=0.03, t(6)=2.84, Student's paired t-test, n=7, distal dendritic locations: 22.68 ± 1.78 ms vs. 28.65 ± 2.17 ms for control vs 50µm ZD-7288 bath application, p=2.1^{-4}, t(8)=-6.39, Student's paired t-test, n=9)**. d.** Schematic illustration of the experimental arrangement. L2/3 PCs were recorded in whole-cell current clamp mode, and a stimulating electrode was placed either in L1 or L4. **e.** I_h modulates EPSP halfwidth for L4 stimulation, but not for L1 (13.87 ± 1.37 ms vs. 15.8 ± 1.67 ms for control vs CsMeSO4 bath application in L1, p=0.38, t(18)=-0.89, Student's two-sample t-test, n=10 each, 10.65 ± 0.64 ms vs.

20.17 ± 2.88 ms for control vs CsMeSO4 bath application in L4, p=0.005, t(18)=-3.22, Student's two-sample t-test, n=10 each, 11.01 ± 0.85 ms vs. 17.05 ± 2.41 ms for control vs CsMeSO4 bath application for putative LGN events, p=0.03, t(18)=-2.36, Student's two-sample t-test, n=10 each). **f.** Pathway-specific I_h effect on unitary EPSP voltage integral (9.35 ± 2.54 mV*ms vs. 12.9 ± 2.04 mV*ms for control vs CsMeSO4 bath application in L1, p=0.3, t(19)=-1.07, Student's two-sample t-test, n=11 and n=10 respectively, 7.85 ± 1.24 mV*ms vs. 17.39 ± 2.5 mV*ms for control vs CsMeSO4 bath application in L4, p=0.002, t(20)=-3.6, Student's two-sample t-test, n=12 and n=10 respectively, 28.01 ± 3.45 mV*ms vs. 44.89 ± 6.42 mV*ms for control vs CsMeSO4 bath application for putative LGN events, p=0.03, t(18)=-2.31, Student's two-sample t-test, n=10 each). **g.** Representative recordings of 50 Hz repeated extracellular stimuli (L1 – grey, L4 – blue, putative LGN -green). **h.** Temporal summation of L4 stimulation in control conditions (black) and during CsMeSO4 application (red). **i.** Pathway-specific I_h modulation of synaptic summation (81.05 ± 14.5 mV*ms vs. 71.07 ± 11.19 mV*ms for control vs CsMeSO4 bath application in L1, p=0.6, t(18)=0.54, Student's two-sample t-test, n=10 each, 60.06 ± 9.03 mV*ms vs. 95.15 ± 11.29 mV*ms for control vs CsMeSO4 bath application in L4, p=0.03, t(18)=-2.42, Student's two-sample t-test, n=10 each, 182.08 ± 23.36 mV*ms vs. 182.05 ± 28.59 mV*ms for control vs CsMeSO4 bath application for putative LGN events, p=0.99, t(18)=$8.74*10^{-4}$, Student's two-sample t-test, n=10 each).

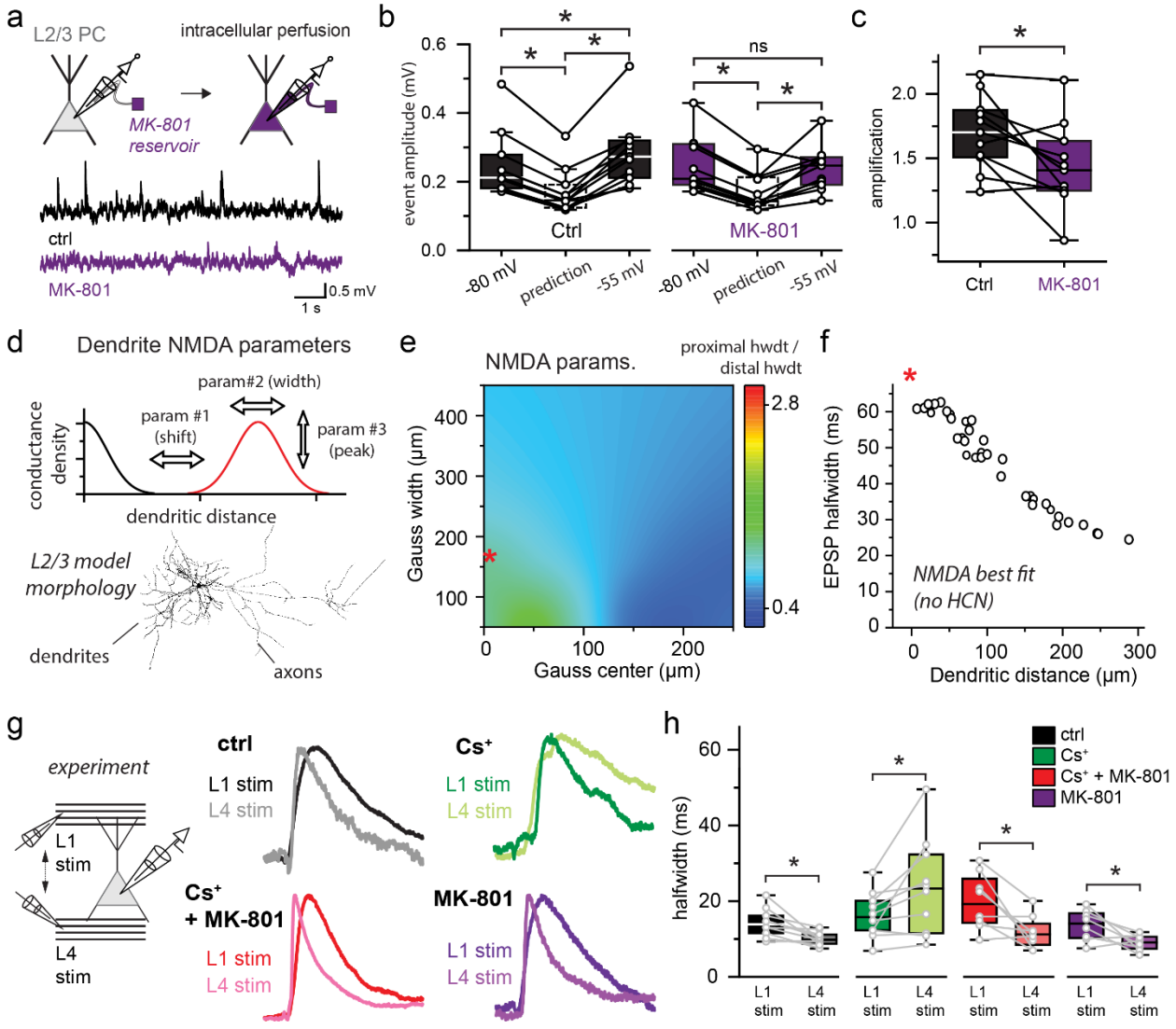

Fig 4. Pathway-specific NMDA receptor boosting of synaptic information

a. Schematic illustration of intracellular pipette solution perfusion during whole-cell patch clamp recordings. Briefly, the pipette was filled with control recording solution (black trace), which was exchanged to an intracellular solution containing 50 µM MK-801 (purple trace) during the recording. **b.** Mean peak amplitude of sEPSPs measured at two different membrane potentials and two different recording conditions (ctrl -80 mV vs. ctrl prediction: $p=4.72*10^{-6}$, $t(10) = 8.86$, ctrl -80 mV vs ctrl -55 mV: $p=0.02$, $t(10) = -2.81$, ctrl prediction vs ctrl -55 mV: $p=1.63*10^{-5}$, $t(10) = -7.71$, MK-801 -80 mV vs. MK-801 prediction: $p=1.15*10^{-6}$, $t(10) = 10.36$, MK-801 -80 mV vs MK-801 -55 mV: $p=0.58$, $t(10) = 0.57$, MK-801 prediction vs MK-801 -55 mV: $p=2.69*10^{-3}$, $t(10) = -3.95$, Student's paired-sample t-test, n = 11 for each). **c.** Synaptic amplification estimated by dividing the predicted peak

amplitude from the hyperpolarized recordings and the measured peak at depolarized membrane potentials (1.69 ± 0.09 and 1.43 ± 0.1 for ctrl and MK-801 amplification respectively, p=0.01, t(10) = 3.04, Student's paired-sample t-test, n=11). **d.** Schematic illustration of the multiparameter NEURON fitting procedure for dendritic NMDA. To cover feasible conductance distributions, the localization of channels along the somato-dendritic axis was set by a Gaussian curve, which was shifted in space, in peak and in width as well (top). Simulations were carried out using fully reconstructed L2/3 PC dendrite from the Allen Institute open-source database (bottom). **e.** Inserting NMDA receptors into proximally located simulated synapses recreates experimentally determined distance-halfwidth relationship. **f.** Best fit of the distance-dependent EPSP halfwidth changes (without HCN). Red asterisk denotes the best fit parameter-space on panel **e. g.** Amplitude-normalized EPSPs recorded from L2/3 PCs by minimal stimulation in either in L1 (dark color tones) or L4 (light color tones) in different recording conditions (ctrl: *black*, extracellular cesium: *green*, extracellular cesium + intracellular MK-801: *red*, intracellular MK-801: *purple*). **h.** The broadening effect of cesium is reversed by NMDA receptor block (14.25 ± 1.17 ms and 10.11 ± 0.56 ms for L1 vs L4 stimuli in control conditions, $p=6.73*10^{-3}$, t(9)=3.5, Student's paired-sample t-test, n=10 each, 16.22 ± 1.91 ms and 23.61 ± 4.04 ms for L1 vs L4 stimuli during Cs bath application, p=0.03, t(9)=-2.67, Student's paired-sample t-test, n=10 each, 19.92 ± 2.65 ms and 11.8 ± 1.55 ms for L1 vs L4 stimuli during Cs bath application and MK-801 intracellular application, p=0.02, t(7)=3.01, Student's paired-sample t-test, n=8 each, 13.62 ± 1.43 ms and 8.97 ± 0.72 ms for L1 vs L4 stimuli during MK-801 intracellular application, p=0.025, t(7)=2.84, Student's paired-sample t-test, n=8 each).

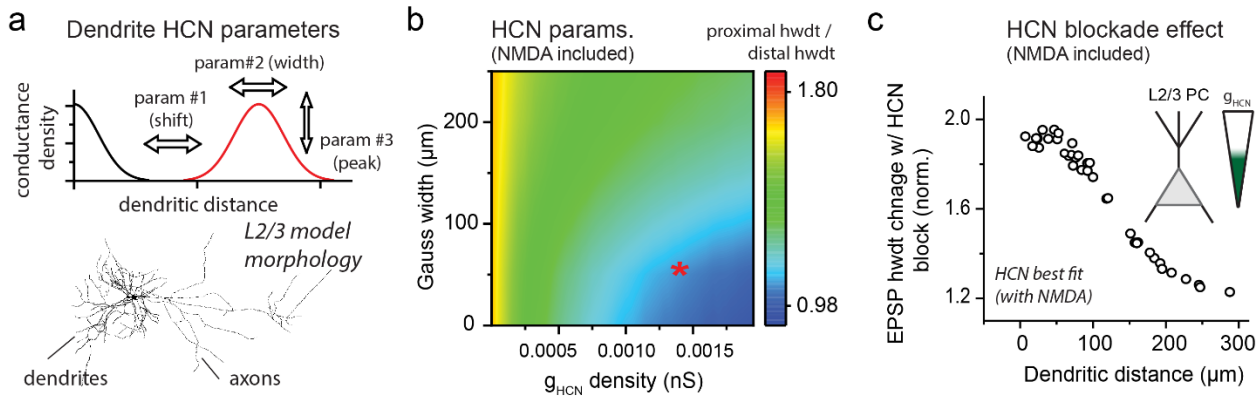

Fig 5. Proximal bias in HCN channel expression dampens NMDA receptor dependent synaptic boosting in a NEURON model simulation.

a. Schematic illustration of the multiparameter NEURON fitting procedure for dendritic HCN, analogous to Fig 4. Simulations included the NMDA dendritic parameters established in Fig. 4. **b**. Proximal abundance of HCN channels recapitulates experimental findings in control conditions. Best fit in the parameter space (denoted with red asterisk) not only recapitulated EPSP halfwidth change, but also our observations regarding changes in input resistance and resting membrane potential. **c.** Schematic illustration of the proposed proximal HCN channel abundance in L2/3 PCs is noted.

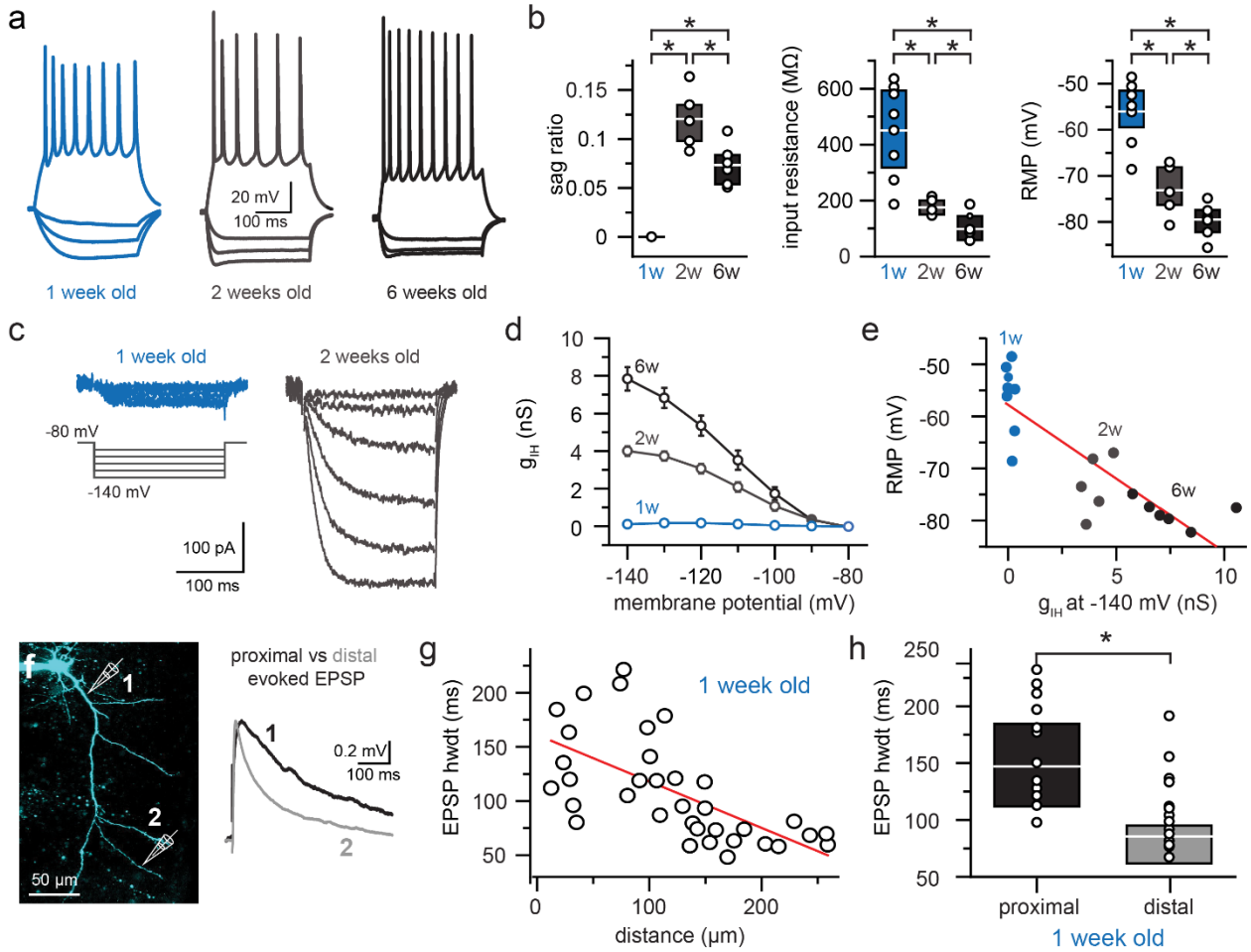

Fig 6. Developmental regulation of I_h expression

a. Representative firing patterns recorded from one week old (left, blue), two weeks old (middle, grey) and six weeks old L2/3 PCs. **b.** Developmental regulation of sag ratio (0.0 ± 0.0, 0.12 ± 0.01 and 0.07 ± 0.01 for one- (n=8), two- (n=5) and six week old L2/3 PCs (n=6), respectively, p=0 for one week old vs two weeks old cells, p=0.01, t(9)=3.04 for two vs six weeks old cells and p=0 for one vs six weeks old cells, Student's two-sample t-test), input resistance (450.6 ± 57.91 MΩ, 175.66 ± 13.66 MΩ and 98.34 ± 18.86 MΩ for one- (n=8), two- (n=5) and six week old L2/3 PCs (n=7), respectively, p=0.004, t(11)=3.65 for one week old vs two weeks old cells, p=0.01, t(10)=3.06 for two vs six weeks old cells and p=1.11*10^{-4}, t(13)=5.54 for one vs six weeks old cells, Student's two-sample t-test) and resting membrane potential (-56.05 ± 2.33 mV, -73.13 ± 2.55 mV and -79.47 ± 1.33 MΩ for one- (n=8), two- (n=5) and six week old L2/3 PCs (n=7), respectively, p=5.9*10^{-4}, t(11)=4.76 for one week old vs two weeks old cells, p=0.04, t(10)=2.39 for two vs six weeks old cells and p=1.36*10^{-6}, t(13)=8.37 for one vs six weeks old cells, Student's two-sample t-test). **c.** Representative voltage clamp recordings of

hyperpolarization activated currents in one week old (left, blue), two weeks old (middle, gray) and six weeks old L2/3 PCs (right, black). **d.** Voltage dependence of hyperpolarization activated currents in one week old (blue), two weeks old (gray) and six weeks old L2/3 PCs (black). **e.** Negative correlation between measured hyperpolarization activated current and resting membrane potential during development (Linear fit (red) slope: -2.84 mV/nS, intercept: -57.67 mV, R^2=0.71, n=20). **f.** Two-photon microscopy image depicting a proximal and a distal extracellular stimulating location positioned closely to an Alexa-594 filled L2/3 PC dendrite (left), and the resulting EPSPs (proximal – black, distal – green). **g.** EPSP halfwidth decreases with dendritic distance (Linear fit (red) slope: -0.42 ms/µm, intercept: 161.01 ms, R^2=0.4, n=35). **h.** EPSPs were significantly slower in proximal dendritic locations (147.07 ± 12.87 ms and 85.57 ± 6.83 ms for proximal and distal events, respectively, $p=5.31*10^{-5}$, t(33)=4.64, Student's two-sample t-test, n=13 and 22, respectively).

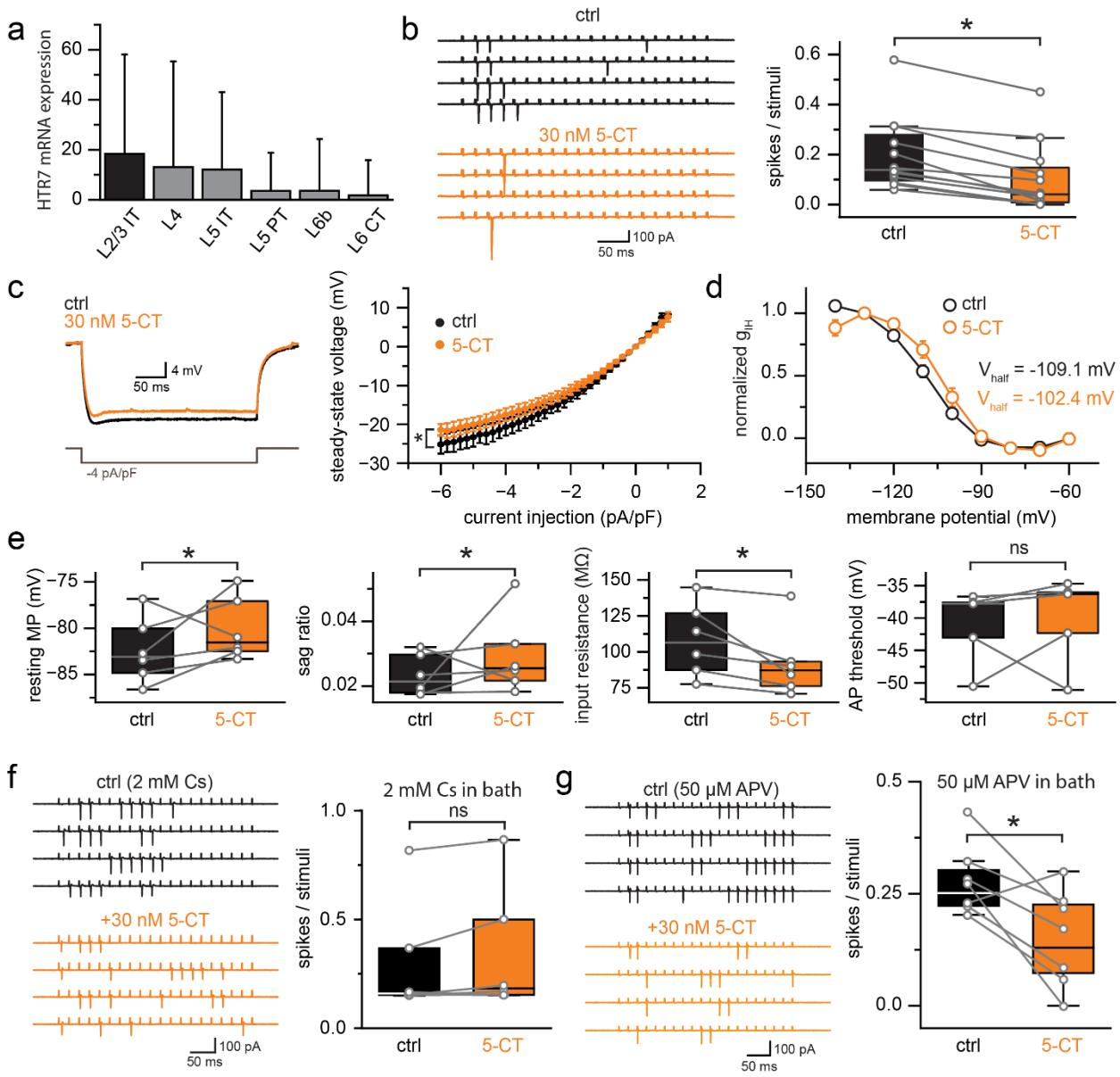

Fig 7. Neuromodulation shifts L2/3 PC excitability via HCN channels

a. $5HT_7$ receptor mRNA is abundantly expressed in L2/3 PCs. Data is collected from the online available dataset(23). **b.** Example cell attached recording of a L2/3 PC (left) upon 50 Hz extracellular stimulation in L4 in control conditions (black) and 5-CT bath application (orange). 5-CT significantly reduced L2/3 PC spiking (0.2 ± 0.04 spike/stimuli vs. 0.1 ± 0.04 spike/stimuli for control vs 5-CT application, $p=3.57*10^{-6}$, t(11)=7.92, Student's paired-sample t-test, n=12 each) **c.** Example current clamp recording of voltage responses to hyperpolarizing current injections (left; control – black, 5-CT – orange). Steady-state voltage response rectification is amplified by $5HT_7R$ blockade (right). **d.** 5-CT shifts the voltage dependence of hyperpolarization activated currents (-109.06 ± 0.47 mV vs -102.35

± 1.09 mV half activation for control vs 5-CT bath application, R^2 = 0.99 for both). **e.** 5-CT did not alter resting membrane potential (-82.41 ± 1.43 mV vs -80.14 ± 1.38 mV in control vs 5-CT bath application, respectively, p=0.89, t(5)=-1.41, Student's paired-sample t-test, n=6 each), sag ratio (0.02 ± $2.55*10^{-3}$ vs 0.03 ± 0.01 in control vs 5-CT bath application, respectively, p=0.82, t(5)=-1.01, Student's paired-sample t-test, n=6 each) and action potential threshold (-41.13 ± 2.6 mV, -40.08 ± 3.05 mV in control vs 5-CT bath application, respectively, p=0.64, t(4)=-0.4, Student's paired-sample t-test, n=5 each), but significantly reduced input resistance (108.21± 10.3 mΩ, 92.29 ± 9.9 MΩ in control vs 5-CT bath application, respectively, p=0.02, t(5)=2.75, Student's paired-sample t-test, n=6 each). **f.** Example recording showing no effect of 5-CT bath application when HCN channels were blocked (left: example recordings, right: 0.3 ± 0.11 spike/stimuli vs 0.34 ± 0.12 spike/stimuli in control vs 5-CT bath application, respectively, p=0.13, t(5)=-1.81, Student's paired-sample t-test, n=6 each). **g.** NMDA independent 5-CT effect on L2/3 PC excitability (0.27 ± 0.03 spike/stimuli vs 0.14 ± 0.04 spike/stimuli in control vs 5-CT bath application, respectively, p=0.01, t(7)=3.66, Student's paired-sample t-test, n=7 each).

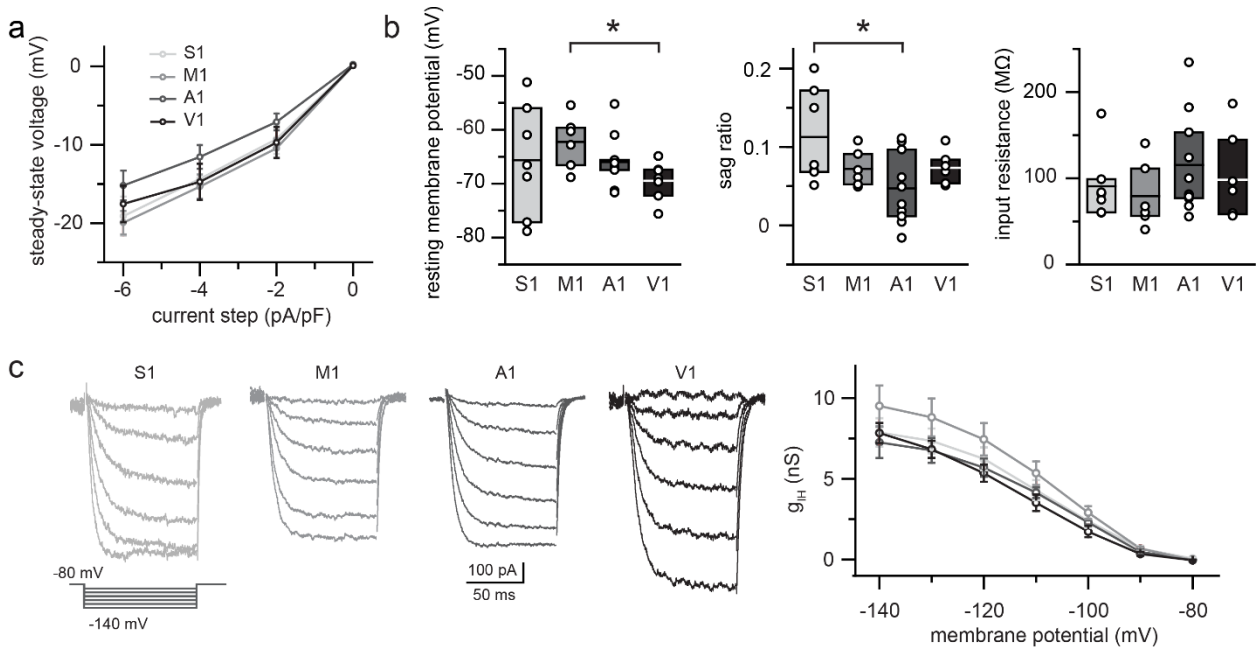

Supplementary Figure 1. Similar Ih current and effect in different cortical areas.

a. Steady-state rectification of L2/3 PCs in the primary somatosensory cortex (S1), primary motor cortex (M1), primary auditory cortex (A1) and primary visual cortex (V1). **b.** Similar resting membrane potential (left), sag ratio (middle) and input resistance (right) of L2/3 PCs in different cortical areas. **c**. Example hyperpolarization activated current recordings from four cortical areas (left), with similar voltage dependent activation (right).

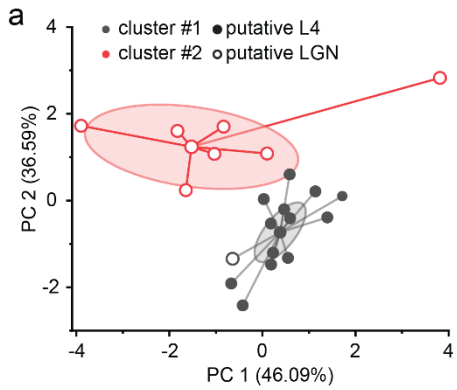

Supplementary Figure 2. Putative LGN and L4 inputs are well separated by k-means clustering

k-means clustering results plotted along the first and second principal component. Ellipses denote the confidence interval; edges are connected to the cluster center. Hollow circles represent putative LGN inputs and filled circles represent L4 inputs determined by the experimenter.

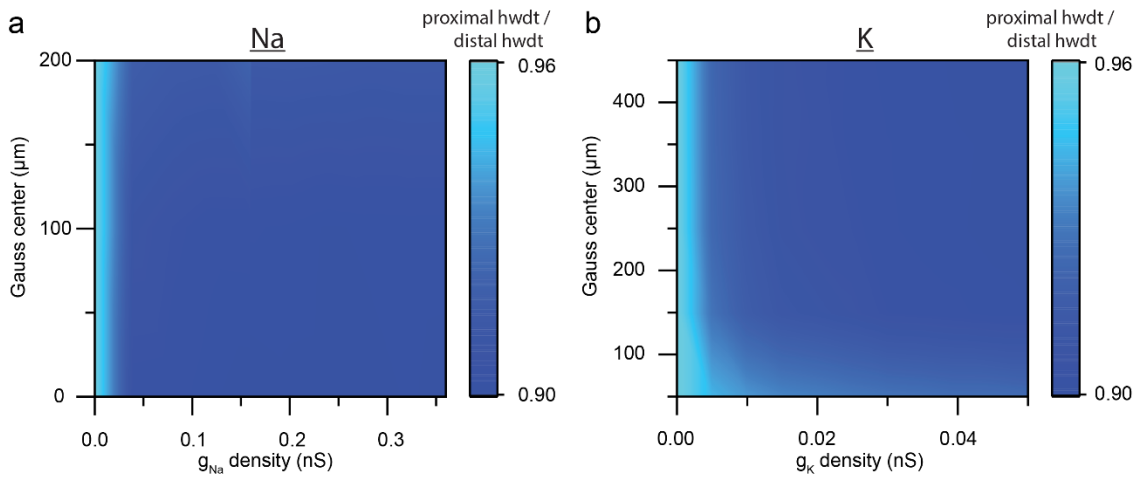

Supplementary Figure 3. The presence of dendritic sodium and potassium channels cannot explain wider proximal synaptic inputs

a. Sodium channels cannot explain the distance-EPSP halfwidth relationship observed when I_h was blocked. Color coding denotes the ratio between proximal and distal EPSP halfwidths. Notice the miniscule range of the color coding. **C.** Same as panel **b.** but for voltage dependent potassium channels.

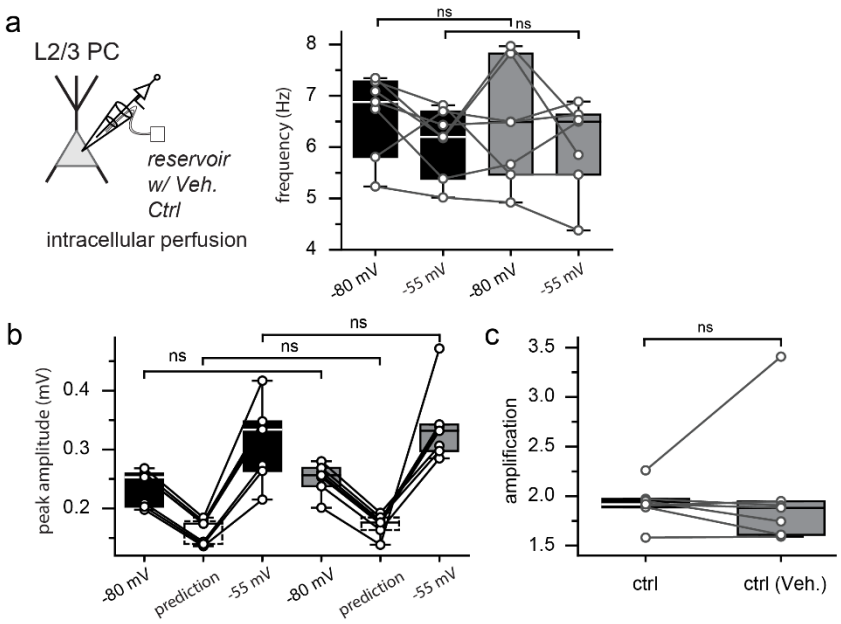

Supplementary Figure 4. Pipette perfusion does not alter spontaneous circuit activity measurements

a. sEPSP frequency is unaltered by pipette perfusion (6.63 ± 0.3 and 6.4 ± 0.44 for ctrl -80 mV and perfused ctrl -80 mV, p=0.57, t(6) = 0.59, 6.1 ± 0.25 and 6.03 ± 0.33 for ctrl -55 mV and perfused ctrl -55 mV, p=0.83, t(6) = 0.23, n=7 for each, Student's paired-sample t-test). **b.** sEPSP peak amplitudes are stable during pipette perfusion experiments (0.23 ± 0.01 and 0.25 ± 0.01 for ctrl -80 mV and perfused ctrl -80 mV, p=0.43, t(6) = -0.83, 0.16 ± 0.01 and 0.17 ± 0.01 for ctrl prediction and perfused prediction, p=0.43, t(6) =-0.83, 0.31 ± 0.03 and 0.34 ± 0.02 for ctrl -55 mV and perfused ctrl -55 mV, p=0.24, t(6) = -1.31, n=7 each, Student's paired-sample t-test). **c.** Pipette perfusion does not alter measured synaptic amplification (1.92 ± 0.07 and 2.01 ± 0.24 for ctrl and perfused ctrl, p=0.65, t(6) = -0.48, n=7 each, Student's paired-sample t-test).

REFERENCES

1. Quiquempoix M, Fayad SL, Boutourlinsky K, Leresche N, Lambert RC, Bessaih T. Layer 2/3 pyramidal neurons control the gain of cortical output. Cell reports. 2018;24(11):2799-807. e4.
2. Wilson DE, Whitney DE, Scholl B, Fitzpatrick D. Orientation selectivity and the functional clustering of synaptic inputs in primary visual cortex. Nature neuroscience. 2016;19(8):1003-9.
3. Hage TA, Bosma-Moody A, Baker CA, Kratz MB, Campagnola L, Jarsky T, et al. Synaptic connectivity to L2/3 of primary visual cortex measured by two-photon optogenetic stimulation. Elife. 2022;11:e71103.
4. Ding Z, Fahey PG, Papadopoulos S, Wang E, Celii B, Papadopoulos C, et al. Functional connectomics reveals general wiring rule in mouse visual cortex. bioRxiv. 2023:2023.03. 13.531369.
5. Scholl B, Wilson DE, Jaepel J, Fitzpatrick D. Functional logic of layer 2/3 inhibitory connectivity in the ferret visual cortex. Neuron. 2019;104(3):451-7. e3.
6. Scholl B, Fitzpatrick D. Cortical synaptic architecture supports flexible sensory computations. Current opinion in neurobiology. 2020;64:41-5.
7. Goetz L, Roth A, Häusser M. Active dendrites enable strong but sparse inputs to determine orientation selectivity. Proceedings of the National Academy of Sciences. 2021;118(30):e2017339118.
8. Smith SL, Smith IT, Branco T, Häusser M. Dendritic spikes enhance stimulus selectivity in cortical neurons in vivo. Nature. 2013;503(7474):115-20.
9. Ujfalussy BB, Makara JK, Lengyel M, Branco T. Global and multiplexed dendritic computations under in vivo-like conditions. Neuron. 2018;100(3):579-92. e5.
10. Landau AT, Park P, Wong-Campos JD, Tian H, Cohen AE, Sabatini BL. Dendritic branch structure compartmentalizes voltage-dependent calcium influx in cortical layer 2/3 pyramidal cells. Elife. 2022;11:e76993.
11. Ferrarese L, Jouhanneau J-S, Remme MW, Kremkow J, Katona G, Rózsa B, et al. Dendrite-specific amplification of weak synaptic input during network activity in vivo. Cell reports. 2018;24(13):3455-65. e5.
12. Luo H, Hasegawa K, Liu M, Song W-J. Comparison of the upper marginal neurons of cortical layer 2 with layer 2/3 pyramidal neurons in mouse temporal cortex. Frontiers in Neuroanatomy. 2017;11:115.
13. Stuart GJ, Spruston N. Dendritic integration: 60 years of progress. Nature neuroscience. 2015;18(12):1713-21.
14. Takahashi N, Oertner TG, Hegemann P, Larkum ME. Active cortical dendrites modulate perception. Science. 2016;354(6319):1587-90.
15. Suzuki M, Larkum ME. General anesthesia decouples cortical pyramidal neurons. Cell. 2020;180(4):666-76. e13.
16. Xu N-l, Harnett MT, Williams SR, Huber D, O'Connor DH, Svoboda K, et al. Nonlinear dendritic integration of sensory and motor input during an active sensing task. Nature. 2012;492(7428):247-51.
17. Shah MM. Cortical HCN channels: function, trafficking and plasticity. The Journal of physiology. 2014;592(13):2711-9.
18. Lörincz A, Notomi T, Tamás G, Shigemoto R, Nusser Z. Polarized and compartment-dependent distribution of HCN1 in pyramidal cell dendrites. Nature neuroscience. 2002;5(11):1185-93.
19. Wahl-Schott C, Biel M. HCN channels: structure, cellular regulation and physiological function. Cellular and molecular life sciences. 2009;66:470-94.
20. Benarroch EE. HCN channels: function and clinical implications. Neurology. 2013;80(3):304-10.
21. Nolan MF, Dudman JT, Dodson PD, Santoro B. HCN1 channels control resting and active integrative properties of stellate cells from layer II of the entorhinal cortex. Journal of Neuroscience. 2007;27(46):12440-51.

822 22. Williams SR, Stuart GJ. Site independence of EPSP time course is mediated by dendritic I h in
823 neocortical pyramidal neurons. Journal of neurophysiology. 2000;83(5):3177-82.
824 23. Gouwens NW, Sorensen SA, Baftizadeh F, Budzillo A, Lee BR, Jarsky T, et al. Integrated
825 morphoelectric and transcriptomic classification of cortical GABAergic cells. Cell. 2020;183(4):935-53. e19.
826 24. Harnett MT, Magee JC, Williams SR. Distribution and function of HCN channels in the apical
827 dendritic tuft of neocortical pyramidal neurons. Journal of Neuroscience. 2015;35(3):1024-37.
828 25. Magee JC. Dendritic Ih normalizes temporal summation in hippocampal CA1 neurons. Nature
829 neuroscience. 1999;2(6):508-14.
830 26. Vetter P, Roth A, Häusser M. Propagation of action potentials in dendrites depends on dendritic
831 morphology. Journal of neurophysiology. 2001;85(2):926-37.
832 27. Malinow R. Transmission between pairs of hippocampal slice neurons: quantal levels, oscillations,
833 and LTP. Science. 1991;252(5006):722-4.
834 28. Yang W, Carrasquillo Y, Hooks BM, Nerbonne JM, Burkhalter A. Distinct balance of excitation and
835 inhibition in an interareal feedforward and feedback circuit of mouse visual cortex. Journal of
836 Neuroscience. 2013;33(44):17373-84.
837 29. Balcioglu A, Gillani R, Doron M, Burnell K, Ku T, Erisir A, et al. Mapping thalamic innervation to
838 individual l2/3 pyramidal neurons and modeling their 'readout'of visual input. Nature Neuroscience.
839 2023;26(3):470-80.
840 30. Sermet BS, Truschow P, Feyerabend M, Mayrhofer JM, Oram TB, Yizhar O, et al. Pathway-, layer-
841 and cell-type-specific thalamic input to mouse barrel cortex. elife. 2019;8:e52665.
842 31. London M, Hausser M. Dendritic computation. Annual review of neuroscience. 2005;28(1):503-
843 32.
844 32. Berger T, Senn W, Lüscher H-R. Hyperpolarization-activated current I h disconnects somatic and
845 dendritic spike initiation zones in layer V pyramidal neurons. Journal of neurophysiology.
846 2003;90(4):2428-37.
847 33. Tsay D, Dudman JT, Siegelbaum SA. HCN1 channels constrain synaptically evoked Ca2+ spikes in
848 distal dendrites of CA1 pyramidal neurons. Neuron. 2007;56(6):1076-89.
849 34. Billeh YN, Cai B, Gratiy SL, Dai K, Iyer R, Gouwens NW, et al. Systematic integration of structural
850 and functional data into multi-scale models of mouse primary visual cortex. Neuron. 2020;106(3):388-
851 403. e18.
852 35. Palmer LM, Shai AS, Reeve JE, Anderson HL, Paulsen O, Larkum ME. NMDA spikes enhance action
853 potential generation during sensory input. Nature neuroscience. 2014;17(3):383-90.
854 36. Branco T, Häusser M. Synaptic integration gradients in single cortical pyramidal cell dendrites.
855 Neuron. 2011;69(5):885-92.
856 37. Bucurenciu I, Kulik A, Schwaller B, Frotscher M, Jonas P. Nanodomain coupling between Ca2+
857 channels and Ca2+ sensors promotes fast and efficient transmitter release at a cortical GABAergic
858 synapse. Neuron. 2008;57(4):536-45.
859 38. Cornford JH, Mercier MS, Leite M, Magloire V, Häusser M, Kullmann DM. Dendritic NMDA
860 receptors in parvalbumin neurons enable strong and stable neuronal assemblies. Elife. 2019;8:e49872.
861 39. Dodt HU, Frick A, Kampe K, Zieglgänsberger W. NMDA and AMPA receptors on neocortical
862 neurons are differentially distributed. European journal of Neuroscience. 1998;10(11):3351-7.
863 40. Guet-McCreight A, Chameh HM, Mahallati S, Wishart M, Tripathy SJ, Valiante TA, et al. Age-
864 dependent increased sag amplitude in human pyramidal neurons dampens baseline cortical activity.
865 Cerebral Cortex. 2023;33(8):4360-73.
866 41. Santello M, Nevian T. Dysfunction of cortical dendritic integration in neuropathic pain reversed
867 by serotoninergic neuromodulation. Neuron. 2015;86(1):233-46.
868 42. Dori I, Dinopoulos A, Blue M, Parnavelas J. Regional differences in the ontogeny of the
869 serotonergic projection to the cerebral cortex. Experimental neurology. 1996;138(1):1-14.

870 43. Vasefi MS, Yang K, Li J, Kruk JS, Heikkila JJ, Jackson MF, et al. Acute 5-HT7 receptor activation
871 increases NMDA-evoked currents and differentially alters NMDA receptor subunit phosphorylation and
872 trafficking in hippocampal neurons. Molecular brain. 2013;6:1-9.
873 44. Megıas M, Emri Z, Freund T, Gulyas A. Total number and distribution of inhibitory and excitatory
874 synapses on hippocampal CA1 pyramidal cells. Neuroscience. 2001;102(3):527-40.
875 45. Nevian T, Larkum ME, Polsky A, Schiller J. Properties of basal dendrites of layer 5 pyramidal
876 neurons: a direct patch-clamp recording study. Nature neuroscience. 2007;10(2):206-14.
877 46. Hubel DH, Wiesel TN. Brain mechanisms of vision. Scientific American. 1979;241(3):150-63.
878 47. Hubel DH, Wiesel TN. Brain and visual perception: the story of a 25-year collaboration: Oxford
879 University Press; 2004.
880 48. Scholl B, Thomas CI, Ryan MA, Kamasawa N, Fitzpatrick D. Cortical response selectivity derives
881 from strength in numbers of synapses. Nature. 2021;590(7844):111-4.
882 49. Waters J, Larkum M, Sakmann B, Helmchen F. Supralinear Ca2+ influx into dendritic tufts of layer
883 2/3 neocortical pyramidal neurons in vitro and in vivo. Journal of Neuroscience. 2003;23(24):8558-67.
884 50. Major G, Polsky A, Denk W, Schiller J, Tank DW. Spatiotemporally graded NMDA spike/plateau
885 potentials in basal dendrites of neocortical pyramidal neurons. Journal of neurophysiology.
886 2008;99(5):2584-601.
887 51. Harris JA, Mihalas S, Hirokawa KE, Whitesell JD, Choi H, Bernard A, et al. Hierarchical organization
888 of cortical and thalamic connectivity. Nature. 2019;575(7781):195-202.
889 52. Rowan MJ, Christie JM. Rapid state-dependent alteration in Kv3 channel availability drives flexible
890 synaptic signaling dependent on somatic subthreshold depolarization. Cell reports. 2017;18(8):2018-29.
891 53. Levelt CN, Hübener M. Critical-period plasticity in the visual cortex. Annual review of
892 neuroscience. 2012;35:309-30.
893 54. Bard JA, Zgombick J, Adham N, Vaysse P, Branchek TA, Weinshank RL. Cloning of a novel human
894 serotonin receptor (5-HT7) positively linked to adenylate cyclase. Journal of Biological Chemistry.
895 1993;268(31):23422-6.
896 55. Karmarkar UR, Dan Y. Experience-dependent plasticity in adult visual cortex. Neuron.
897 2006;52(4):577-85.
898 56. Hensch TK, Bilimoria PM, editors. Re-opening windows: manipulating critical periods for brain
899 development. Cerebrum: the Dana forum on brain science; 2012: Dana Foundation.
900 57. Nolan MF, Malleret G, Dudman JT, Buhl DL, Santoro B, Gibbs E, et al. A behavioral role for dendritic
901 integration: HCN1 channels constrain spatial memory and plasticity at inputs to distal dendrites of CA1
902 pyramidal neurons. Cell. 2004;119(5):719-32.
903 58. Wu J, El-Hassar L, Datta D, Thomas M, Zhang Y, Jenkins DP, et al. Interaction Between HCN and
904 Slack Channels Regulates mPFC Pyramidal Cell Excitability and Working Memory. bioRxiv. 2023:2023.03.
905 04.529157.
906 59. Yu L, Tasaki S, Schneider JA, Arfanakis K, Duong DM, Wingo AP, et al. Cortical proteins associated
907 with cognitive resilience in community-dwelling older persons. JAMA psychiatry. 2020;77(11):1172-80.
908 60. Ramírez D, Zúñiga R, Concha G, Zúñiga L. HCN channels: new therapeutic targets for pain
909 treatment. Molecules. 2018;23(9):2094.
910 61. Ku SM, Han M-H. HCN channel targets for novel antidepressant treatment. Neurotherapeutics.
911 2017;14(3):698-715.
912 62. Kim CS, Johnston D. A possible link between HCN channels and depression. Chronic Stress.
913 2018;2:2470547018787781.
914 63. Postea O, Biel M. Exploring HCN channels as novel drug targets. Nature reviews Drug discovery.
915 2011;10(12):903-14.

916 64. Lyman KA, Han Y, Chetkovich DM. Animal models suggest the TRIP8b-HCN interaction is a
917 therapeutic target for major depressive disorder. Expert Opinion on Therapeutic Targets. 2017;21(3):235-
918 7.
919 65. Fukuyama K, Motomura E, Okada M. Therapeutic potential and limitation of serotonin type 7
920 receptor modulation. International Journal of Molecular Sciences. 2023;24(3):2070.
921 66. Ishibashi T, Horisawa T, Tokuda K, Ishiyama T, Ogasa M, Tagashira R, et al. Pharmacological profile
922 of lurasidone, a novel antipsychotic agent with potent 5-hydroxytryptamine 7 (5-HT7) and 5-HT1A
923 receptor activity. Journal of Pharmacology and Experimental Therapeutics. 2010;334(1):171-81.
924 67. Shimizu M, Mi X, Toyoda F, Kojima A, Ding W-G, Fukushima Y, et al. Propofol, an Anesthetic Agent,
925 Inhibits HCN Channels through the Allosteric Modulation of the cAMP-Dependent Gating Mechanism.
926 Biomolecules. 2022;12(4):570.
927 68. Chen X, Shu S, Kennedy DP, Willcox SC, Bayliss DA. Subunit-specific effects of isoflurane on
928 neuronal I h in HCN1 knockout mice. Journal of neurophysiology. 2009;101(1):129-40.
929 69. Taylor AL. What we talk about when we talk about capacitance measured with the voltage-clamp
930 step method. Journal of computational neuroscience. 2012;32(1):167-75.
931 70. Desai NS, Gray R, Johnston D. A dynamic clamp on every rig. eneuro. 2017;4(5).
932 71. Oláh VJ, Tarcsay G, Brunner J. Small size of recorded neuronal structures confines the accuracy in
933 direct axonal voltage measurements. Eneuro. 2021;8(4).
934 72. Testa-Silva G, Rosier M, Honnuraiah S, Guzulaitis R, Megias AM, French C, et al. High synaptic
935 threshold for dendritic nmda spike generation in human layer 2/3 pyramidal neurons. Cell reports.
936 2022;41(11).

937